Nanoscale



PAPER



Cite this: Nanoscale, 2017, 9, 5164

Ion selective redox cycling in zero-dimensional nanopore electrode arrays at low ionic strength†

Kaiyu Fu, Da Donghoon Han, Chaoxiong Ma and Paul W. Bohn **D** ** **D** **D**

Surface charge characteristics and the electrical double layer (EDL) effect govern the transport of ions into and out of nanopores, producing a permselective concentration polarization, which dominates the electrochemical response of nanoelectrodes in solutions of low ionic strength. In this study, highly ordered, zero-dimensional nanopore electrode arrays (NEAs), with each nanopore presenting a pair of recessed electrodes, were fabricated to couple EDL effects with redox cycling, thereby achieving electrochemical detection with improved sensitivity and selectivity. These NEAs exhibit current amplification as high as 55-fold due to the redox cycling effect, which can be further increased by ~500-fold upon the removal of the supporting electrolyte. The effect of nanopore geometry, which is a key factor determining the magnitude of the EDL effect, is fully characterized, as is the effect of the magnitude and sign of the charge of the redox-active species. The observed changes in limiting current with the concentration of the supporting electrolyte confirm the accumulation of cations and repulsion of anions in NEAs presenting negative surface charge. Exploiting this principle, dopamine was selectively determined in the presence of a 3000-fold excess of ascorbic acid within the NEA.

Received 9th January 2017, Accepted 10th March 2017 DOI: 10.1039/c7nr00206h

rsc.li/nanoscale

Introduction

Molecular transport and reactions within structures with nanometer size confinement can improve electrochemical analyses yielding enhanced sensitivity in a miniaturized platform. 1-3 Recently, the rapid development of nanofabrication techniques has enabled the design and construction of advanced nanostructures which can exploit the transport of charged molecules under nanoscale confinement and with nanometer-scale control of the electric field.^{4,5} For example, the integration of electrodes with nanostructures allows electrochemical measurements to be conducted on small length and volume scales with enhanced mass transport, negligible iR drop, and small charging currents, thus enabling fast scan rates. 6-8

Among the universe of nanoelectrode architectures, nanopore-based electrodes are especially interesting, because they mimic biological nanopores embedded in cell membranes, and because they can effectively utilize the special properties of ion transport near charged surfaces and molecular interactions within ultrasmall volumes. 9-11 Glass nanopore electrodes^{12,13} and solid-state nanopores, ^{14,15} for example, have been

used to observe chemical and biochemical processes, e.g. DNA translocation 16,17 and protein adsorption/desorption, 18,19 with single molecule sensitivity. Synthetic nanopores not only approach the small size of biological nanopores but also exhibit multiple functionality, for example after chemical modification, 20,21 thus allowing in situ observation by fluorescence microscopy^{22,23} and electrochemical imaging.^{24,25} One unique characteristic of nanopore electrodes is that molecules can be trapped in the nanostructure and their transport and reactivity can be controlled by the strong intrinsic electric field inside the pore. 26,27 These principles can be used to simplify and enhance electrochemical analysis and enable the integration of nanoscale lab-on-a-chip devices. 28-30 However, it is crucial that mass transport in these confined nanostructures be well-understood in order to realize miniaturized high sensitivity electrochemical sensing platforms.

The surface charge of nanopores and nanochannels has been shown to be a key governing factor controlling the transport of ionic species. 31,32 It has been widely observed that counterions are accumulated, while co-ions are repelled, in a manner determined by the charge density of the nanopore surface, the ionic strength in the solution (as measured through the Debye length, κ), and the pore/channel size, d. ^{33,34} The surface charge can thus be used to manipulate ion distributions and improve the ion selectivity in nanochannels.^{35,36} It has also been found that the surface charge can significantly alter electrochemical behavior at nanopore electrodes by controlling mass transport. 13,37 The exterior and interior surfaces

^aDepartment of Chemistry and Biochemistry, University of Notre Dame, Notre Dame, IN 46556, USA. E-mail: pbohn@nd.edu

^bDepartment of Chemical and Biomolecular Engineering, University of Notre Dame, Notre Dame, IN 46556, USA

[†]Electronic supplementary information (ESI) available. See DOI: 10.1039/ c7nr00206h

of nanopores can be chemically modified to produce the desired charge, which then enables the pore to serve as an ion gate to modulate the transport of redox molecules by adjusting the solution pH. Recently, White and coworkers demonstrated this idea in a nanogap electrochemical cell by investigating the transport of redox molecules in solutions with low electrolyte concentrations by measurements and simulations of the concentration distribution and voltammetric behavior within the nanochannel. ^{38,39}

While electrical double layer (EDL) effects alone at nanoelectrodes lead to increases in faradaic currents, we have previously demonstrated that combining EDL effects with redox cycling at nanopore electrode arrays (NEAs) can produce an additional current amplification as large as ~100-fold. 40,41 Ion accumulation in negatively charged NEAs is the dominant contribution to this significant current amplification. Herein, we explore EDL effects in zero-dimensional recessed ring-disk electrode NEAs, viz. Fig. 1(A), for selective electrochemical detection, focusing in particular on how the geometry of the nanopore and the charge of the species combine to determine accumulation or repulsion of redox species in nanopores. The dependence of the EDL effect on the NEA geometry is investigated by varying the nanopore size and the depth to which the electrode is recessed in the nanopores using Ru(NH₃)₆³⁺ as a model analyte. Smaller nanopores and thicker SiO2 spacer layers lead to a stronger EDL effect, which facilitates ion accumulation. The voltammetry of four representative analytes with different redox-variable charge states is evaluated on the

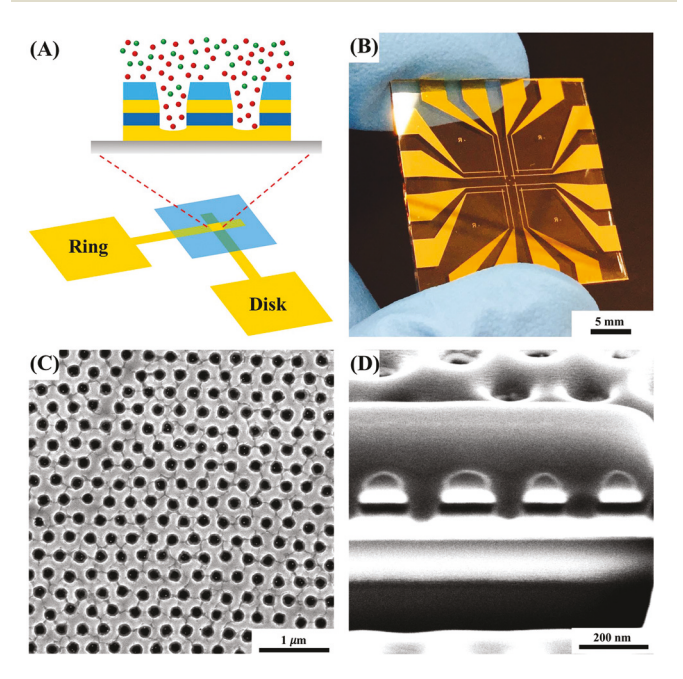


Fig. 1 (A) Schematic diagram showing the layout of nanopore electrode arrays (NEAs), with each nanopore containing a recessed ring-disk electrode pair in the vertical direction (inset). (B) Photo of an electrochemical chip holding 8 pairs of dual-electrode sensor arrays. (C) Plane view and (D) side view SEM images of NEAs. The white, black and grey layers in (D) indicate gold, SiN_x , and SiO_2 , respectively.

NEAs at different ionic strengths. The results confirm the screening of anions and accumulation of cations. Exploiting this concept, the selectivity for electrochemical determination of dopamine (DA) in the presence of a negatively charged interferent, ascorbic acid (AA), was determined to be \sim 3000 fold.

Experimental section

Chemicals and materials

Hexaammineruthenium(III) chloride ([Ru(NH₃)₆]Cl₃), ferrocenium hexafluorophosphate (FcPF₆), potassium hexacyanoruthenate(II) hydrate (K₄[(Ru(CN)₆)]), sodium anthraquinone-2-sulfonate (AQMS), dopamine (DA), ascorbic acid (AA), and potassium chloride (KCl) were obtained from Sigma-Aldrich and used as received. Deionized (DI) water (18 M Ω cm) purified using a Millipore Milli-Q system was used to prepare all aqueous solutions for electrochemical measurements.

Device fabrication

NEAs with a recessed ring-disk geometry were fabricated using a combination of photolithography, layer-by-layer metal deposition, nanosphere lithography (NSL), and reactive ion etching, similar to previously reported procedures. 42 The macroscale layout of the device is shown in Fig. 1(B). The nanopore electrode arrays (150 μ m × 150 μ m) are defined at the intersection of top and bottom electrode layers. Plane view and cross-sectional SEM images of the nanopore electrode arrays are given in Fig. 1(C) and (D), respectively. Here the thickness of the layers from top to bottom are 100-500 nm (SiO₂), 100 nm (Au), 60 nm (SiN_x) and 100 nm (Au). The spacing and diameter of the nanopores were controlled by varying the size of polystyrene nanospheres used in NSL and the exposure time to O2 plasma etching, respectively.42 The SiO2 thickness was controlled by the time of plasma-enhanced chemical vapor deposition (PECVD).

Modeling and calculations

The voltammetric response of $Ru(NH_3)_6^{3/2+}$ and $Ru(CN)_6^{4/3-}$ redox cycling in NEAs was modeled using finite element simulation software (COMSOL Multiphysics 5.2). Briefly, the mass transport was described by the Nernst–Planck equation,

$$\frac{\partial C_i}{\partial t} = \nabla \cdot D_i \left[\nabla C_i + \frac{z_i F}{RT} C_i \nabla \Phi \right] \tag{1}$$

where F is the Faraday's constant, R is the gas constant, T = 298.15 K is the absolute temperature, Φ is the electric potential, and D_i , C_i and z_i are the diffusion coefficient, concentration, and charge of the species $i \left(\text{Ru(NH}_3)_6^{3/2+}, \text{Ru(CN)}_6^{4/3-}, \text{K}^+, \text{Cl}^- \right)$.

Poisson's equation was used to calculate the electric potential

$$\nabla^2 \Phi = \frac{\rho}{\varepsilon_0 \varepsilon_{\rm R}} \tag{2}$$

Paper Nanoscale

where ε_0 and ε_R are the permittivity of space and the dielectric constant of the medium, respectively. The space charge density, ρ , in eqn (2) is determined by the concentration of charged species in the solution via,

$$\rho = F \sum_{i} z_i C_i \tag{3}$$

Combining eqn (1)–(3) produces the Poisson–Nernst–Planck equations, which govern molecular transport and electric field strength in the NEA geometry.

A model NEA of 10 nanopores was simulated in a 2D geometry, consisting of recessed disk electrodes, a 60 nm thick insulating layer, a 100 nm thick ring electrode layer, and a top insulator layer of variable thickness. The pore size and pore spacing used in the simulations were 250 nm and 300 nm, respectively. The domain above the pores was drawn sufficiently large ($w = 1000 \ \mu m$, $h = 1000 \ \mu m$) to avoid interference from boundaries, and the mesh was refined both within the nanopores and in the region just above the pores to provide sufficient resolution. Details of the computational methods used in the simulations can be found in the ESI.†

Characterization

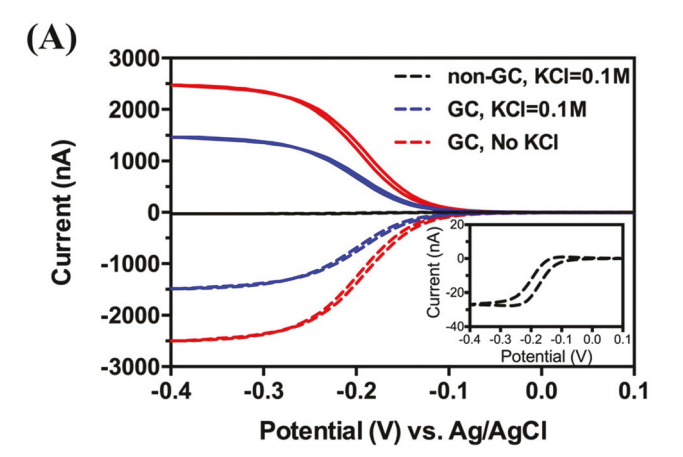
Scanning electron microscopy (SEM) images were obtained by using a FEI-Helios Dual Beam FIB at an accelerating voltage of 5 kV. Prior to SEM imaging, all samples were sputter-coated with 2.5 nm iridium to avoid surface charging. Cyclic voltammetry (CV) was performed on a CHI bipotentiostat (CH Instruments, Model 842C). The top and bottom electrodes of the NEAs were operated as first and second working electrodes, respectively. All potentials are reported νs . Ag/AgCl at 300 K, unless noted otherwise. During electrochemical measurements, the Pt wire counter and Ag/AgCl reference electrodes were immersed in a 200 μ L solution inside a PDMS reservoir. In all CV measurements, the top electrodes were either held at a constant potential (GC mode) or disconnected (non-GC mode), while the potential of the bottom electrode in the array was scanned at 100 mV s⁻¹.

Results and discussion

NEA fabrication and redox cycling behavior

The nanopore electrode arrays (NEAs) with a recessed ring-disk dual electrode structure are shown schematically in Fig. 1(A). The NEAs were fabricated using previously reported procedures, ⁴² such that each device consisted of 8 pairs of individually addressable dual-electrode NEAs as shown in Fig. 1(B). Each of the 8 arrays measured 150 μ m × 150 μ m with pore densities ranging from 10 pores per μ m² to 0.04 pores per μ m². Fig. 1(C) shows a plane view SEM image of a typical NEA. In the arrays, each nanopore housed a 100 nm Au top ring electrode separated by a 60 nm insulating SiN_x layer from the bottom Au disk electrode, as shown in the SEM cross section image in Fig. 1(D).

Cyclic voltammetry (CV) was conducted on the NEAs to test the efficiency of redox cycling using the bottom disk as the generator electrode and the top ring as the collector. Fig. 2(A) shows the CV of 1 mM $Ru(NH_3)_6^{3+}$ in 0.1 M aqueous KCl on NEAs with a pore size (D_p) of ~250 nm and a pore spacing (S_p) of 300 nm. In these experiments the bottom electrode was swept from -0.4 V to 0.1 V, while the top electrode was held at +0.1 V (GC mode) or allowed to float (non-GC mode). The limiting currents (i_L) obtained from the GC mode and non-GC mode were 1.49 µA and 27 nA, respectively, yielding an amplification factor from redox cycling, AF_{RC} = 55. The collection efficiency, determined by the ratio of the collector (top), $i_{\rm C}$, to generator (bottom), i_G , current, was $\geq 99\%$. The high collection efficiency and strong resulting current amplification can be attributed to the architecture of the NEAs. First, the generator is surrounded by a collector electrode ~60 nm away within a small diameter nanopore, meaning that reaction products from the bottom electrode can be efficiently captured by the



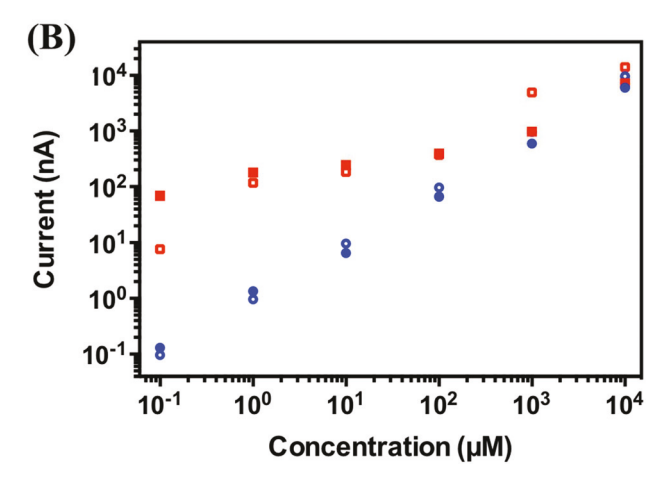


Fig. 2 (A) Cyclic voltammograms of 1 mM ${\rm Ru(NH_3)_6}^{3+}$ on the NEAs obtained by sweeping the bottom electrode while holding the top electrode at 0.1 V either with (blue) or without (red) 0.1 M KCl, or floating the top electrode in 0.1 M KCl (black). Top electrode (solid) and bottom electrode currents (dashed) displayed. (Inset) Magnified CV obtained with the top electrode floating. (B) Experimental (solid) and simulated (open) limiting currents obtained in GC-mode for different concentrations of ${\rm Ru(NH_3)_6}^{3+}$ with 0.1 M KCl (blue) or without KCl (red).

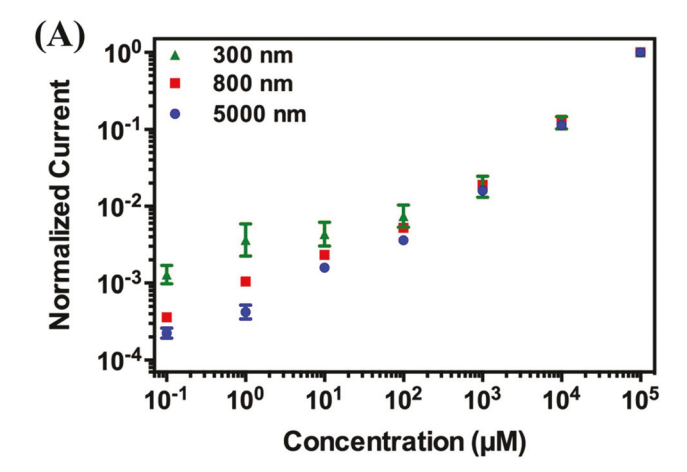
ring electrodes before diffusing into the bulk. In addition, the small inter-electrode distance allows rapid transport of redox species between the two electrodes.

Furthermore, i_L obtained on the NEAs in the absence of the supporting electrolyte (red curve in Fig. 2(A)) shows a ~70% increase relative to that obtained in 0.1 M KCl. Both ion accumulation and migration inside NEAs have been shown to contribute to this additional current amplification. 40 At sufficiently low ionic strength, the thickness of the EDL is comparable to the nanopore in size, resulting in EDL overlap. At sufficiently low ionic strength, the surface charge of the nanopores cannot be completely screened by the counter-ions resulting in a strong coupling to the transport of the charged redox species. In the absence of the supporting electrolyte, the EDL effect depends entirely on the analyte concentration which determines the ionic strength and the resulting Debye length. Of course, the Debye length and the EDL are also influenced by the surface charge density inside the nanopores, but the commonly employed methods to control surface charge, e.g. pH control by a buffer system, are precluded by the need to keep the ionic strength low.

Limiting currents obtained with varying concentrations of $\text{Ru}(\text{NH}_3)_6^{3+}$ in the presence (i_{SE}) and absence (i_{ASE}) of the supporting electrolyte (SE) are given in Fig. 2(B). Consistent with theory, in 0.1 M KCl i_{SE} depends linearly on the analyte concentration over the entire concentration range, 100 nM to 10 mM. However, while i_{ASE} agrees well with i_{SE} at high, >1 mM, analyte concentration, significant differences are observed below 1 mM, an effect which can be attributed to the increasing EDL overlap as the concentration is lowered. At the lowest concentration (lowest ionic strength), 0.1 μ M, i_{ASE} is ~500 fold larger than i_{SE} . Accumulation of cationic Ru(NH₃)₆³⁺ in the permselective nanopores is the major contribution to this additional current amplification with unscreened ion migration also playing a smaller role. 41 Simulated limiting currents from NEAs of 10 nanopores were calculated and scaled by the ratio of experimental to simulated pores = 22 500 for comparison with experimental i_L values. As shown in Fig. 2(B), the simulated limiting currents from Ru(NH₃)₆³⁺ in the presence of KCl (blue, open symbols) agree very well with the experimental data (blue, solid symbols). In the absence of KCl, the simulated limiting currents (red, open symbols) also reproduce the experimentally observed deviation from linearity with a concentration of $Ru(NH_3)_6^{3+}$.

Effect of NEA geometry on ion transport

Conductance experiments in nanochannels and nanopores have shown that the EDL effect and resulting ion accumulation or screening depend on the size of the channel. The dependence of the EDL effect on voltammetry in the NEA geometry was investigated using $\mathrm{Ru}(\mathrm{NH_3})_6^{3^+}$ in the absence of SE. Fig. 3(A) shows the normalized i_L obtained at varying concentrations of $\mathrm{Ru}(\mathrm{NH_3})_6^{3^+}$ in the absence of SE obtained on the NEAs with three different pore diameters. Similar to the results in Fig. 2, i_L changes linearly with the concentration of $\mathrm{Ru}(\mathrm{NH_3})_6^{3^+}$ at high concentrations (>1 mM) independent of



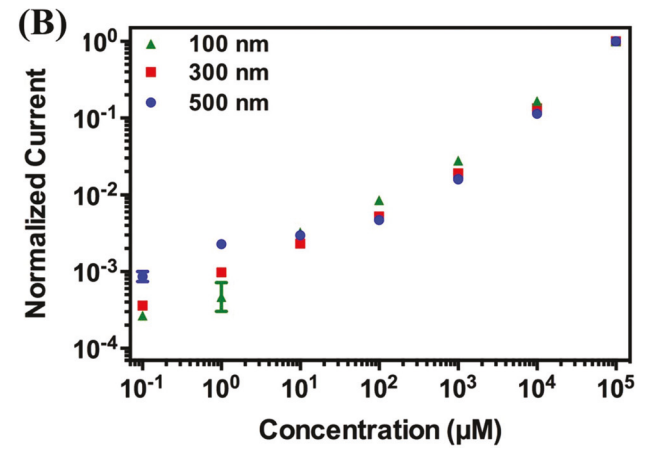


Fig. 3 Normalized limiting current as a function of concentration of Ru(NH₃)₆³⁺ in the absence of KCl obtained from NEAs with different pore sizes, D_D , (A), and top SiO₂ spacer layer thickness, T_D (B).

 $D_{\rm p}$. Deviations from linearity are observed below 1 mM for all three $D_{\rm p}$ values, with the largest non-linearities being observed for the smallest $D_{\rm p}$ values, as expected based on the ion accumulation effect. The strong dependence on the pore diameter arises, because the surface charge to pore volume ratio is larger for smaller pores. Accordingly, ion accumulation and the EDL effect increase with decreasing pore size. Consequently, Fig. 3(A) shows that the NEAs with a $D_{\rm p}$ of 300 nm produce a ~10-fold larger $i_{\rm L}$ than NEAs with a $D_{\rm p}$ of 5 µm, consistent with the behavior of ion transport in nanochannels.³⁵

To further elucidate the effect of nanopore geometry on ion accumulation, the distance by which the ring-disk electrode pair was recessed from the bulk solution was investigated by varying the thickness (T_p) of the top SiO_2 layer and conducting the voltammetry of $\mathrm{Ru}(\mathrm{NH}_3)_6^{3^+}$ in the absence of SE. As shown in Fig. 3(B), stronger EDL effects and larger i_L values are observed in NEAs with larger T_p values. The magnitude of i_L increases almost 10-fold as T_p changes from 100 nm to 500 nm at concentrations $\leq 1~\mu\mathrm{M}~\mathrm{Ru}(\mathrm{NH}_3)_6^{3^+}$. However, in the high concentration range, i_L for NEAs with $T_p = 500~\mathrm{nm}$ was slightly smaller than for those with T_p values of 300 nm and

Paper Nanoscale

100 nm. This is likely due to the conical shape of the nanopores, *i.e.* the effective electrode area of NEAs with a $T_{\rm p}$ of 500 nm is smaller than NEAs with smaller $T_{\rm p}$ values, resulting in a smaller current.

Effect of analyte charge

To further characterize the role of the negatively charged surface in ion transport, reversible redox species of different charge states were investigated on the NEAs at varying ionic strengths. The CVs of $Ru(NH_3)_6^{3+}$, ferrocenium (Fc⁺), anthra-

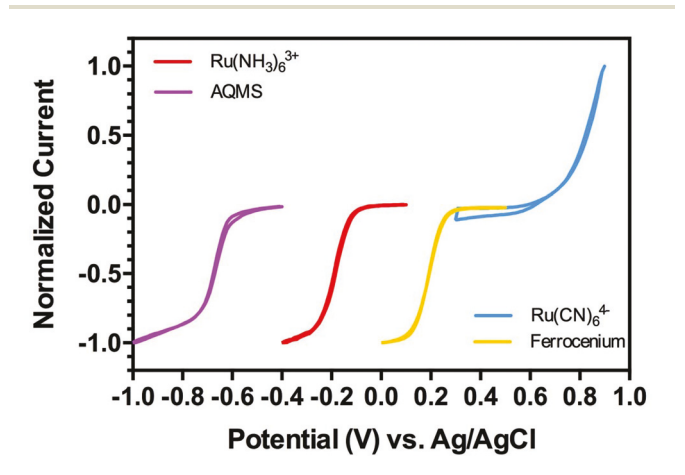


Fig. 4 Cyclic voltammograms on NEAs for the four redox systems used in this work with a sweep rate of 100 mV s $^{-1}$. Current was normalized to the steady-state current.

quinone-2-sulfonate (AQMS⁻), and $\operatorname{Ru}(\operatorname{CN})_6^{4-}$ are given in Fig. 4. The half wave potentials ($E_{1/2}$) of these redox species are also listed in Table S1.† In all measurements, the top electrode was fixed at the oxidation (reduction) potential of the reduced (oxidized) member of the redox pair, while the bottom electrode was swept at 100 mV s⁻¹. Under these experimental conditions (pH 7), the charges of the redox species and their corresponding electrochemical reactions are

$$Ru(NH_3)_6^{3+} + e^- \rightarrow Ru(NH_3)_6^{2+}$$
 (4)

$$Fc^+ + e^- \rightarrow Fc$$
 (5)

$$Ru(CN)_6^{4-} - e^- \to Ru(CN)_6^{3-}$$
 (6)

$$AQMS^{-} - e^{-} \rightarrow AQMS \tag{7}$$

Fig. 5 shows the limiting currents of the CVs of these redox pairs as a function of SE concentration in the range [KCl] = 1 μ M to 1 M. Fig. 5(A) shows that $i_{\rm L}$ of Ru(NH₃)₆³⁺ at 10 μ M and 100 μ M increases with decreasing SE concentration. Comparison of $i_{\rm ASE}$ to $i_{\rm SE}$ indicates ~9- and ~27-fold current increases for Ru(NH₃)₆³⁺ at 100 μ M and 10 μ M, respectively. This result is consistent with the data in Fig. 2 and previous observations, ⁴¹ since the ionic strength at 10 μ M Ru(NH₃)₆³⁺ is smaller than that of 100 μ M Ru(NH₃)₆³⁺ in the absence of SE. The simulations (blue, open symbols) reproduce the trend that positive analytes produce a larger current signal with decreasing ionic strength. A similar trend is observed for Fc⁺/Fc with changing ionic strength, indicating 5- and 6-fold current increases respectively at 100 μ M and 10 μ M, in the absence of SE, Fig. 5(B). The smaller current enhancement in the Fc⁺/Fc

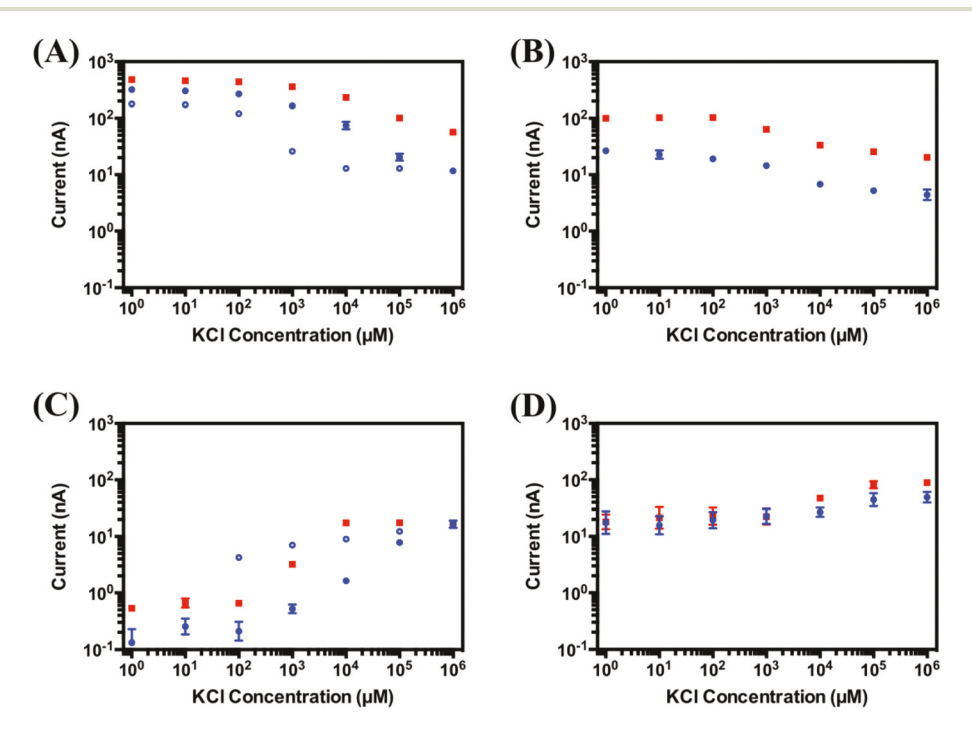


Fig. 5 Experimental (solid) and simulated (open) limiting currents obtained from four redox pairs at two different redox species concentrations (red, 100 μ M and blue, 10 μ M) as a function of KCl concentration. The redox systems used were (A) Ru(NH₃)₆³⁺, (B) Fc⁺, (C) Ru(CN)₆⁴⁻, and (D) AQMS.

system at low ionic strength, relative to $Ru(NH_3)_6^{2/3+}$ likely reflects the fact that Fc^+ , but not Fc is accumulated in the negatively charged nanopores, confirming the key role of charge interactions in the ion accumulation effect.

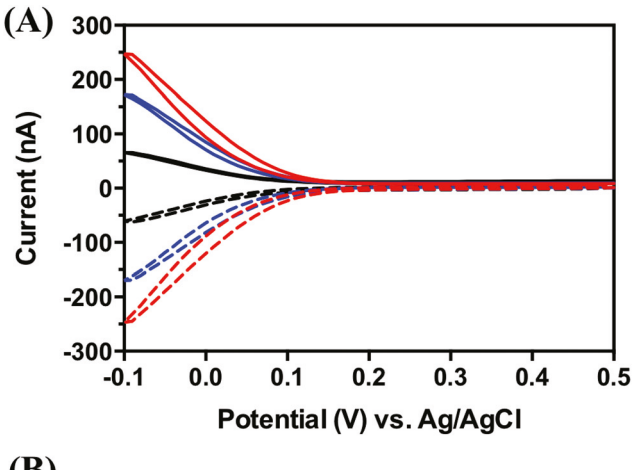
The dependence of the ion accumulation effect on the negatively charged surface was further confirmed by conducting the CVs of anions, $Ru(CN)_6^{4-}$, Fig. 5(C), and AQMS⁻, Fig. 5(D). In contrast to the behavior of the positively charged redox pairs, the i_L values of both ions decrease with decreasing SE concentration, which is expected, since these anionic reactants are repelled by the negatively charged nanopore surface. These results are also consistent with ion screening effects observed in nanochannels and in nanopore-confined electrodes. Again, the magnitude of the ionic charge of the redox couples plays an important role in the ion screening effect, as evidenced by the larger decrease of i_L for $Ru(CN)_6^{4-/3-}$ than for AQMS^{0/-} upon the removal of SE. The i_L of 10 μ M $Ru(CN)_6^{4-/3-}$ decreases more than 100-fold with decreasing SE concentration, while the decrease is only 2.8-fold for AOMS^{0/-}.

These results strongly indicate a dominant role for ion permselectivity in determining the electrochemical behavior of nanopore-confined recessed ring-disk electrode pairs. Despite the fact that ion migration effects, impurities in the redox system, and variation of the nanopore surface charge density due to adsorption may confound the observed $i_{\rm L}$ values, the results in Fig. 5 reflect both distinct EDL effects and strong charge dependence of the voltammetry of anionic and cationic redox pairs when measured in NEAs.

Selectivity of NEAs

The above results demonstrate the capacity of NEAs to respond differentially to ions of different charge. In order to test whether this property of NEAs can be used for selective detection of redox species based on their charges, dopamine, DA, and ascorbic acid, AA, were used as model species. DA (p K_a = 8.86) and AA (p K_a = 4.17) are dominantly positively and negatively charged, respectively, at pH 7, and thus would be expected to exhibit different EDL effects on the NEAs. As expected, Fig. 6(A) shows that i_L of DA increases with decreasing KCl concentration, exhibiting a 3.7-fold larger current in the absence of SE than at the highest KCl concentration. This value is smaller than that obtained for Ru(NH₃)₆^{2/3+}, which is consistent with the smaller charge of the DA redox couple. In addition, ion accumulation effects might also be reduced at very low KCl concentrations due to adsorption of DA.⁴³

The resulting $i_{\rm L}$ values of DA and AA as a function of KCl concentration are given in Fig. 6(B). In contrast to the behavior of DA with decreasing ionic strength, the $i_{\rm L}$ of AA drops as the KCl concentration decreases, which can be attributed to the screening effect of the negative nanopore surface on the AA anion at pH 7. Also, the $i_{\rm L}$ obtained for AA is much smaller than DA at 1 M KCl. This is attributed to the irreversibility of the AA which precludes the redox cycling effect and current amplification. Taking the concentration of the two redox species into account, the selectivity of DA *versus* AA is roughly 200-fold at 1 M KCl. This selectivity is further amplified by the



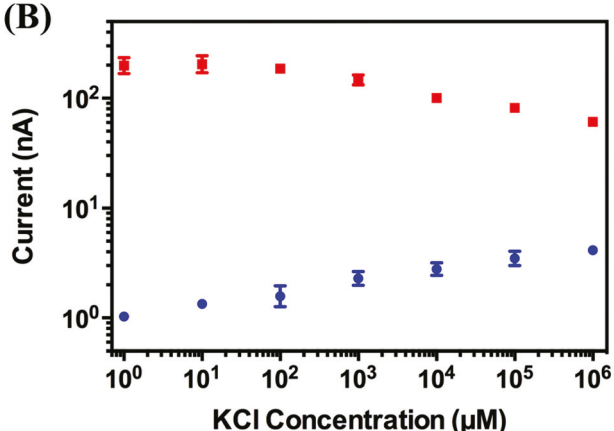


Fig. 6 (A) Cyclic voltammograms of 100 μ M DA with different concentrations of KCl, including 1 μ M (red), 1 mM (blue) and 1 M (black). Top (ring) electrode current (solid) and bottom (disk) electrode current (dashed). (B) Limiting currents obtained from 100 μ M DA (red) and 1500 μ M AA (blue) as a function of KCl SE concentration.

EDL effect with decreasing KCl concentration, reaching 3000-fold at 1 μM KCl. These results confirm that ion screening effects on NEAs may be employed to differentiate analytes based on their charge, demonstrating that electrochemical selectivity can be enhanced significantly when coupling EDL effects with redox cycling of the target analyte, and further establishing NEAs as a promising platform for electrochemical sensing.

Conclusion

In summary, the combination of electrochemical redox cycling and surface charge-dominated ion accumulation within NEAs produces a large ion selectivity for differently charged redox species at low ionic strength. The NEAs used here consist of stacked metal-insulator-metal electrode structures with well-controlled nanopore size and spacing. In these structures current signals are amplified by redox cycling between the recessed ring-disk electrode pairs, and the current can be

Paper Nanoscale

further enhanced by decreasing the concentration of the supporting electrolyte, or operating without any supporting electrolyte at all. This additional signal enhancement in the absence of SE is attributed to ion accumulation (permselectivity) effects within the nanopores of the NEAs. The geometric parameters of NEAs, e.g. pore size and spacing as well as recess depth of the electrode pairs, were carefully tuned to investigate the dependence of ion transport on the nanopore geometry. We found that smaller and more recessed nanopores capture cationic redox species like Ru(NH₃)₆³⁺ more efficiently, resulting in higher limiting currents. Redox pairs with charges of different magnitudes and signs show completely different responses upon decreasing the SE concentration - NEAs tend to screen negatively charged species and trap positively charged redox pairs. Finally, the strong ion accumulation effect observed in these NEAs was used in a proof-of-concept to improve the detection selectivity of the neurotransmitter dopamine in the presence of a predominant electrochemical interference from ascorbic acid. The combination of redox cycling and ion accumulation in this system contributes to a ~3000 fold ion selectivity for detection of dopamine.

Acknowledgements

This work was supported by the National Science Foundation grant 1404744 (K. F. and C. M.) and the Defense Advanced Research Projects Agency FA8650-15-C-7546 (D. H.). Fabrication and structural characterization of the devices studied here were accomplished at the Notre Dame Nanofabrication Facility and the Notre Dame Integrated Imaging Facility, whose support is gratefully acknowledged.

References

- 1 A. Piruska, M. Gong, J. V. Sweedler and P. W. Bohn, *Chem. Soc. Rev.*, 2010, **39**, 1060–1072.
- 2 C. Batchelor-McAuley, E. J. F. Dickinson, N. V. Rees, K. E. Toghill and R. G. Compton, *Anal. Chem.*, 2012, 84, 669–684.
- 3 K. Dawson and A. O'Riordan, *Annu. Rev. Anal. Chem.*, 2014, 7, 163–181.
- 4 J. T. Cox and B. Zhang, Annu. Rev. Anal. Chem., 2012, 5, 253-272.
- 5 Y. Fan, C. Han and B. Zhang, *Analyst*, 2016, **141**, 5474–5487.
- 6 D. W. M. Arrigan, Analyst, 2004, 129, 1157-1165.
- 7 R. W. Murray, Chem. Rev., 2008, 108, 2688-2720.
- 8 S. M. Oja, M. Wood and B. Zhang, *Anal. Chem.*, 2013, **85**, 473–486.
- 9 T. Li, L. Su, W. Hu, H. Dong, Y. Li and L. Mao, *Anal. Chem.*, 2010, **82**, 1521–1526.
- 10 P. Sun, Anal. Chem., 2010, 82, 276-281.
- 11 L. J. Small, D. R. Wheeler and E. D. Spoerke, *Nanoscale*, 2015, 7, 16909–16920.

12 B. Zhang, Y. H. Zhang and H. S. White, *Anal. Chem.*, 2004, **76**, 6229–6238.

- 13 G. L. Wang, B. Zhang, J. R. Wayment, J. M. Harris and H. S. White, *J. Am. Chem. Soc.*, 2006, **128**, 7679–7686.
- 14 A. J. Storm, J. H. Chen, X. S. Ling, H. W. Zandbergen and C. Dekker, *Nat. Mater.*, 2003, **2**, 537–540.
- 15 C. Dekker, Nat. Nanotechnol., 2007, 2, 209-215.
- 16 A. J. Storm, C. Storm, J. H. Chen, H. Zandbergen, J. F. Joanny and C. Dekker, *Nano Lett.*, 2005, 5, 1193– 1197.
- 17 S. M. Iqbal, D. Akin and R. Bashir, *Nat. Nanotechnol.*, 2007, 2, 243–248.
- 18 W. Li, N. A. W. Bell, S. Hernández-Ainsa, V. V. Thacker, A. M. Thackray, R. Bujdoso and U. F. Keyser, *ACS Nano*, 2013, 7, 4129–4134.
- 19 J. Kong, N. A. W. Bell and U. F. Keyser, *Nano Lett.*, 2016, **16**, 3557–3562.
- 20 W. Guo, H. W. Xia, L. X. Cao, F. Xia, S. T. Wang, G. Z. Zhang, Y. L. Song, Y. G. Wang, L. Jiang and D. B. Zhu, Adv. Funct. Mater., 2010, 20, 3561–3567.
- 21 X. Hou, W. Guo and L. Jiang, *Chem. Soc. Rev.*, 2011, 40, 2385–2401.
- 22 S. P. Branagan, N. M. Contento and P. W. Bohn, *J. Am. Chem. Soc.*, 2012, **134**, 8617–8624.
- 23 L. P. Zaino, D. A. Grismer, D. Han, G. M. Crouch and P. W. Bohn, *Faraday Discuss.*, 2015, **184**, 101–115.
- 24 J. H. Bae, Y. Yu and M. V. Mirkin, *J. Phys. Chem. C*, 2016, 120(37), 20651–20658.
- 25 M. Kang, D. Momotenko, A. Page, D. Perry and P. R. Unwin, *Langmuir*, 2016, 32, 7993–8008.
- 26 Y. Kim, K. S. Kim, K. L. Kounovsky, R. Chang, G. Y. Jung, J. J. dePablo, K. Jo and D. C. Schwartz, *Lab Chip*, 2011, 11, 1721–1729.
- 27 R. Tahvildari, E. Beamish, V. Tabard-Cossa and M. Godin, *Lab Chip*, 2015, 15, 1407–1411.
- 28 N. M. Contento, S. P. Branagan and P. W. Bohn, *Lab Chip*, 2011, **11**, 3634–3641.
- 29 D. Fine, A. Grattoni, E. Zabre, F. Hussein, M. Ferrari and X. W. Liu, *Lab Chip*, 2011, 11, 2526–2534.
- 30 E. Choi, K. Kwon, S. J. Lee, D. Kim and J. Park, *Lab Chip*, 2015, 15, 1794–1798.
- 31 B. D. Bath, H. S. White and E. R. Scott, *Anal. Chem.*, 2000, 72, 433–442.
- 32 H. Daiguji, P. Yang and A. Majumdar, *Nano Lett.*, 2004, 4, 137–142.
- 33 D. Krapf, B. M. Quinn, M.-Y. Wu, H. W. Zandbergen, C. Dekker and S. G. Lemay, *Nano Lett.*, 2006, 6, 2531–2535.
- 34 Y. H. Zhang, B. Zhang and H. S. White, *J. Phys. Chem. B*, 2006, **110**, 1768–1774.
- 35 D. Stein, M. Kruithof and C. Dekker, *Phys. Rev. Lett.*, 2004, **93**, 035901.
- 36 R. Karnik, R. Fan, M. Yue, D. Li, P. Yang and A. Majumdar, *Nano Lett.*, 2005, 5, 943–948.
- 37 H. S. White and A. Bund, *Langmuir*, 2008, **24**, 12062–12067.
- 38 J. Xiong, Q. Chen, M. A. Edwards and H. S. White, *ACS Nano*, 2015, **9**, 8520–8529.

39 Q. Chen, K. McKelvey, M. A. Edwards and H. S. White, *J. Phys. Chem. C*, 2016, **120**, 17251–17260.

- 40 C. Ma, N. M. Contento and P. W. Bohn, *J. Am. Chem. Soc.*, 2014, 136, 7225–7228.
- 41 C. Ma, W. Xu, W. R. A. Wichert and P. W. Bohn, *ACS Nano*, 2016, **10**, 3658–3664.
- 42 K. Fu, D. Han, C. Ma and P. W. Bohn, *Faraday Discuss.*, 2016, **193**, 51-64.
- 43 B. Gao, L. Su, H. Yang, T. Shu and X. Zhang, *Analyst*, 2016, 141, 2067–2071.
- 44 C. Ma, N. M. Contento, L. R. Gibson and P. W. Bohn, *Anal. Chem.*, 2013, **85**, 9882–9888.